

685

690

695

PART I

CHAPTER 3: IN-SITU LWC PROBES

3.1 LWC PROBE TYPES

700

In-Situ probes are used to determine the localized LWC of clouds, haze, and fog measuring the LWC at the location of the sensor, rather than remotely as in RADAR, LIDAR, and satellite imagery. In-situ measurements provide us with the most accurate information about cloud characteristics, mostly on scales from 10^{-2} to 10^2 meters. For in cloud measurements these instruments are often mounted on an aircraft, usually under the wings or near the front of the fuselage in such a way that they are kept isolated from major sources of flow distortion.

In-Situ probes employ various methods for measuring LWC. Two of the most common methods are to use a heated element technique to directly measure the LWC from first principles or to derive the LWC from the size distributions measured by optical scattering probes. Each type of in-situ probe has advantages and limitations. This chapter introduces the concepts and details of the theory and operation of the probes that measure LWC either directly or as a derived quantity.

715 3.1.1 HEATED ELEMENT PROBES

Heated element, or “hot-wire” probes utilize a heated wire coil maintained at a constant current or constant temperature (Wendisch & Brenguier, 2013). LWC is

calculated from the power dissipated in the heated wire as it evaporates liquid droplets that impinge upon it (King, 1978). Hot-wire liquid water probes are an adaptation of the hot-wire anemometer, an instrument that measures a fluid's velocity by noting the amount of heat taken away by the fluid by convection. In fact, these probes respond both to liquid water and to moist airflow past the sensing element (Wendisch & Brenguier, 2013). Figure 4 shows an idealization of how droplets interacting with the hot-wire coil's heat field can vaporize droplets.

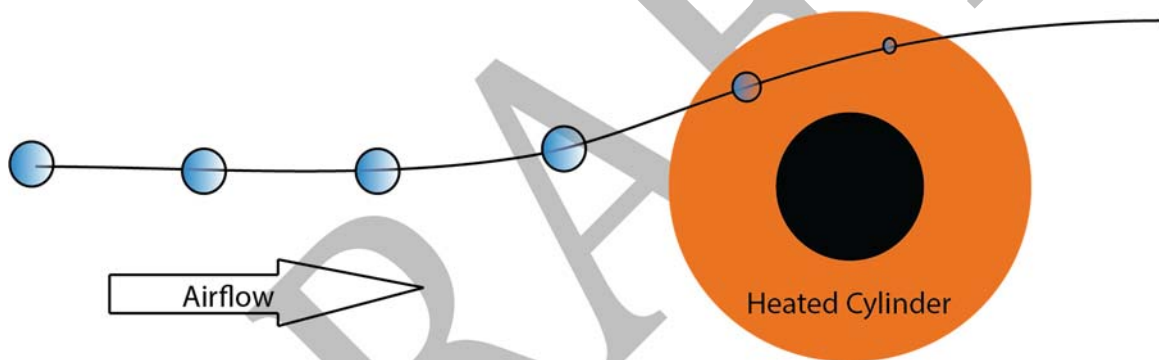


Figure 4: Schematic of how a water droplet in air flow interacts with a hot-wire coil evaporating as it enters the heat field around it. Droplets can either impact the cylinder and form a thin film before evaporating or enter the heat field and evaporate near the cylinder. Both result in a change of resistance of the cylinder requiring more power to be delivered to the wire which allows for calculation of LWC (figure reproduced from Wendisch & Brenguier)

A typical Wheatstone bridge type circuit (Figure 5) is used to determine the change in resistance of the wire that occurs from the temperature change from these two processes. This circuit – in its simplest form – consists of two known resistances, one unknown resistance – that of the hot-wire sensor coil, and a fourth

variable resistance.. While the circuit is in balance, e.g. when the variable resistance and the unknown resistance – e.g. the hot-wire coil – is at its ambient value, the voltage drop between resistor pairs will be zero. When this condition holds, the ratio of the two known resistors is exactly equal to the ratio of adjusted value of variable resistance and the value of unknown resistance.

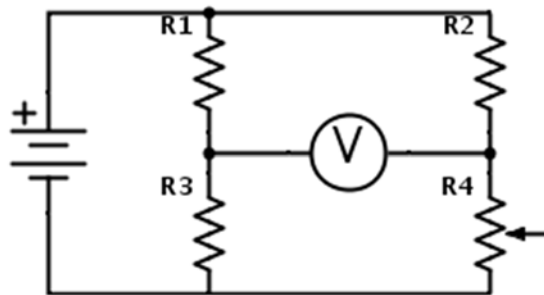


Figure 5: Schematic of a simplified Wheatstone Bridge circuit. The variable resistor is adjusted to rebalance the circuit such that the voltmeter in the center reads zero. This idea is used in determining the power dissipated by the evaporating liquid water droplets as they interact with the hot-wire sensor coil.

When the temperature of the coil changes its resistance due to the convective cooling or evaporation the circuit will go out of balance and there will be a voltage drop between the nodes. The magnitude of the power dissipated, measured by this voltage change, is thus a function of both the LWC in the airstream and the temperature and velocity of the air that is passing over the coil. The regulated power required to keep the wire at a constant temperature is directly related to the amount of power dissipated.

The power dissipated by the probe wire is given by the power lost by the heat losses due to convection, radiation, and the latent heat of vaporization:

$$P = P_{\text{radiative}} + P_{\text{convective}} + P_{\text{evaporative}} \quad (1)$$

The radiative losses are usually negligible so only the convective and evaporative power losses are considered:

$$P = P_{\text{convective}} + P_{\text{evaporative}} \quad (2)$$

765

King's Law generically gives the relationship between power loss, flow velocity, and temperature and is used to determine the power dissipated by the wire (Lomas 1986):

770

$$P = (A + B v^N)(T_w - T_a) \quad (3)$$

775

Here v is the flow velocity of the fluid normal to the wire (e.g. the airspeed of the aircraft), T_w is the wire temperature, T_a is the air (fluid) temperature, and A, B, N are empirical constants, called the King Constants. They are dependent on the properties of the fluid in question. In this case clear and moist air.

The earliest forms of hot-wire probes used on aircraft date back to the 1950's. The Johnson-Williams Liquid Water Content Probe (J-W) determines LWC by the change in electrical current in the hot-wire coil, which is maintained at a constant voltage, as it cooled due to the evaporation of cloud droplets (Neel 1955).

780 However, the J-W probe also suffered from several disadvantages, including that it required a “wet” calibration box and could not be calibrated in dry conditions.

In the late 1970’s King et. al. improved upon the design of the J-W LWC Probe. Their design used a wire maintained at a constantly monitored temperature, rather than at constant voltage. Their design both allowed for the calculation of its response characteristics from first principles but more importantly for calibration in dry conditions. It also addressed issues with axial heat losses, due to conduction, by adding a slave coil at each end of the master coil. The slave coils are maintained at the same temperature as the master, sensing coil. The temperature of the wire must be high enough to efficiently evaporate water before effects like shedding come into play, but low enough to avoid the formation of a vapor barrier between droplets and the wire, which would result in lower collection efficiency (King et. al. 1978).

Applying King’s law to this probe wire we arrive at the following relationship for the power dissipated by the hotwire from the evaporation and convective effects:

$$P = l d \nu LWC [L_v(T) + c_w(T_w - T_a)] + \pi l \kappa (T_w - T_a) Nu. \quad (4)$$

Here, l and d are the length and diameter of the wire respectively, LWC is the liquid water content, $L_v(T)$ is the latent heat of vaporization of liquid water, c_w is the specific heat of liquid water, and κ is the thermal conductivity of air (King et. al. 1978).

The first term is the “wet” term – the heat required to warm and evaporate the droplets – and the second is the dry air term – the heat lost to the fluid flow by convection. Nu is the Nusselt Number, defined as the ratio of the convective to conductive heat transfer normal to the wire/liquid water film boundary and is
805 (Lomas 1986):

$$Nu = \frac{h L}{\kappa}. \quad (5)$$

Here, h is the heat transfer coefficient and L is the characteristic length. For the probe wire moving at aircraft speeds on the order of 100 m/s $Nu = 0.12 d^{0.68}$ (King
810 et. al 1978).

When the Reynolds number, which is the ratio of pressure forces to the shear forces, is within the interval $10^3 < Re < 2 \times 10^5$ it can be shown that

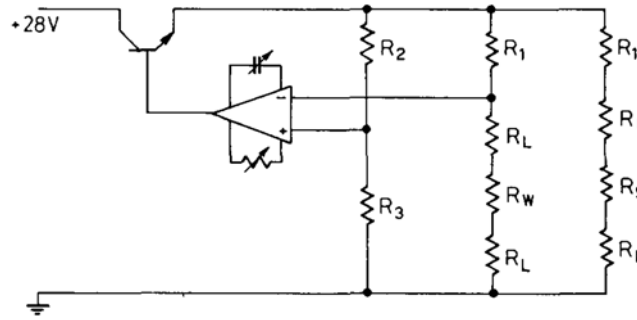
$$Nu = 0.26 Re_f^{0.6} Pr_f^{0.37} \left(\frac{Pr_f}{Pr_w} \right)^{0.25}. \quad (6)$$

815 Here, Re is the Reynolds number, and Pr is the Prandtl number, which is the ratio of kinematic viscosity to thermal diffusivity, for the flow of the medium around the hot-wire coil. The subscripts f and w refer to the free stream flow and the stream flow around the wall of the cylinder respectively (Zakšauskas and Ziugzda 1985).

Once the power dissipated by the hot-wire is known, and the effects of the
820 dry air term are estimated or calculated, the power dissipated by evaporation is all

that remains and in turn can be directly related to the magnitude of the liquid water content (King, et. al. 1978).

The control circuit maintains the hot-wire, R_w , at a constant temperature by maintaining it at a constant resistance. The resistance of the sensing coil decreases
825 as the wire temperature decreases causing the amplifier in the control circuit, shown in Figure 6, to increase the voltage in order to bring the Wheatstone bridge bridge back into balance (King et. al. 1978).



830 *Figure 6: King's hot-wire probe control circuit. It is a slightly more complex version of a standard Wheatstone bridge circuit. (adapted from King, et. al., 1978).*

835 The power dissipated by the circuit, in terms of voltages, V , and resistances, R , is given by (King et. al. 1978):

$$P = \frac{V^2 \left(\frac{R_3 R_1}{R_2} - 2 R_L \right)}{R_1^2 \left(1 + \frac{R_3}{R_2} \right)^2} \quad (7)$$

Setting (7) equal to (4) allows one to determine the LWC directly:

840

$$LWC = \frac{P - P_d}{A v (L_v + c_w(T_w - T_a))} \quad (8)$$

where P is the measured power, given by (7), P_d is the dry-air power term, and A is the sensor area. The convective heat losses, or dry-air term, is calculated by:

845

$$P_d = \pi A_0 \kappa(T_{wire}) Re^x Pr^y \quad (9)$$

where κ is the thermal conductivity and is a function of the wire temperature. Ideally since LWC should be zero in clear air this is a good check to whether or not the wire temperature is too hot or not hot enough (Zakšauskas and Ziugzda 1985).

850

3.1.1.1 THE DMT LWC-100

The LWC-100 probe, manufactured by Droplet Measurement Technologies (DMT), is a modern implementation of the design of the King probe. The basic design remains relatively unchanged, even nearly 40 years later. The greatest difference between the original King probe and the commercially available LWC-100

855

is improved electronic control systems. It also has an anti-icing heating element built into the sensor strut.

The LWC-100's sensing element is 1.8 mm in diameter and 20 mm in length,
860 operates at $\sim 125^{\circ}\text{C}$ as set at the factory[†], and comes as a modular circuit card that
can be easily swapped in and out. The LWC-100 is mounted on a specially designed
strut that can be affixed either to the fuselage or the wing of the aircraft with the
sensing element directed toward the incoming flow. Figure 7 shows the mechanical
drawing of the LWC-100 probe taken from DMT's user manual and Figure 8 shows a
865 photograph of the modular circuit card for the sensor and slave coils.

[†] Each sensor card has a slightly different resistance, so the actual operating temperature is determined through analysis of clear air flight data.

Modular Sensor Circuit Card

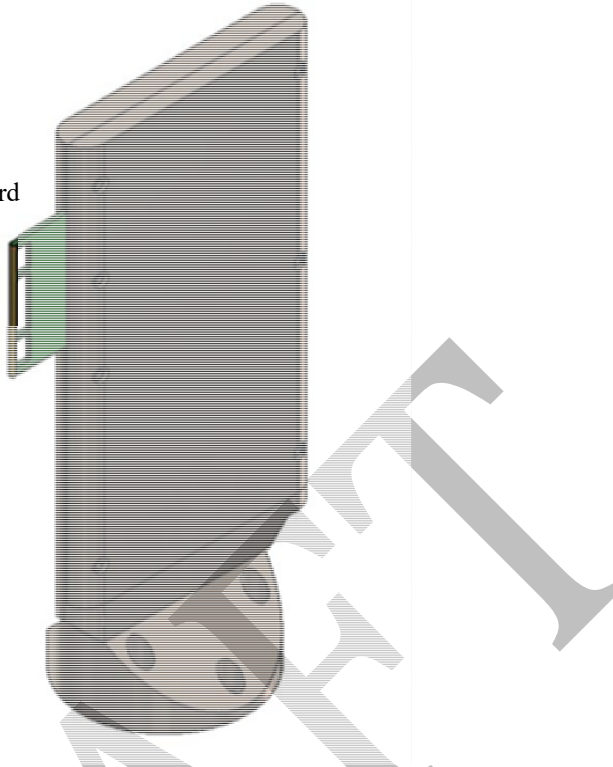


Figure 7: Mechanical drawing of the DMT LWC-100 probe taken from the DMT user manual. The LWC-100 has a 2.5-inch diameter B.C. Rosemount pattern mounting for easy installation on research aircraft.

870



Figure 8: Modular circuit card containing the slave and sensing coils for the DMT LWC-100. The card is designed to be plugged into the main probe housing and to be easily replaceable (Adapted from DMT user manual).

875

Figure 9 shows the more advanced Wheatstone bridge circuit used in the DMT LWC-100 probe. This particular circuit uses a pulse width modulated system of heating and cooling the coil reducing heat dissipation in the power field effect transistors (FET) that heat the master and slave coils. This in turn leads to a lower electronics failure rate (Droplet Measurement Technologies, 2013).

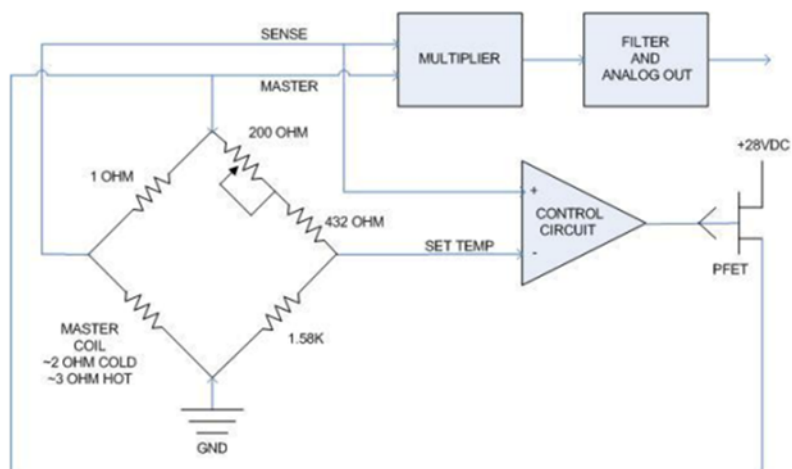


Figure 9: Pulse Width Modulated Wheatstone bridge circuit in the DMT LWC-100. much less heat is dissipated in the power FET's that heat the master and slave coils (adapted from the DMT LWC-200 user's manual).

The LWC-100 is described by DMT, and the University of Wyoming's internal instrumentation documentation, to be able to measure LWC, at 25 Hz, from 0 g/m^3 to 3 g/m^3 . The LWC-100 has an accuracy of 0.2 g/m^3 . Additionally, the manufacturer specifies operating limits for the LWC-100 at between $\pm 40^\circ C$, up to 40,000 ft (~ 12 km) MSL, and airspeeds up to 200 m/s . However, during COPE, as will be shown in Chapter 4, the LWC-100 probe could only effectively measure LWC

up to, on average, $\sim 2.6 \text{ g/m}^3$. Above these volumes, the LWC-100 shows saturation “roll-off.”

895 The LWC-100’s first major limitation is in its ability to effectively measure LWC at the extremes of droplet size spectra. For example, it is limited by collection efficiency considerations on the small end of the droplet size spectrum as droplets with diameter less than about $10 \text{ }\mu\text{m}$ will tend to follow the airflow around the the sensor & not fully evaporate. On the large end of the spectrum, for drops larger than
900 $50\mu\text{m}$, incomplete evaporation due to factors such as impact, shatter, and shedding – where water is carried away by the airstream before sufficient heat has been transferred to vaporize them – can occur. Thus, for both small and large drops one expects the LWC-100 to underestimate the LWC.

 The second major limitation of the LWC-100 its inability to compensate for
905 changes in flow angle. Figure 10 illustrates how the airflow may be different relative to the sensing element of the LWC-100. In the cases where the flow angle changes, the dry-air power term increases but this is not accounted for in calculations so residual power is assumed to be due to evaporation of LWC. The LWC calculated in those cases, therefore shows a noticeable increase. This typically occurs in cases
910 where the sideslip angle, the angle between the forward movement of the aircraft and the relative wind, increases negatively. Figure 11 shows an out-of-cloud segment of the July 9, 2013 calibration flight that took place during COPE. The jump in LWC is on the order of between 0.10 and 0.15 g/m^3 for sideslip angles increasing negatively from 0 to -5 degrees. Figure 12 shows a scatterplot between the aircraft sideslip and

915 LWC showing that there is a correlation between the two. These “jumps” in LWC
have not been compensated for in the processing of the COPE data for the LWC-100.

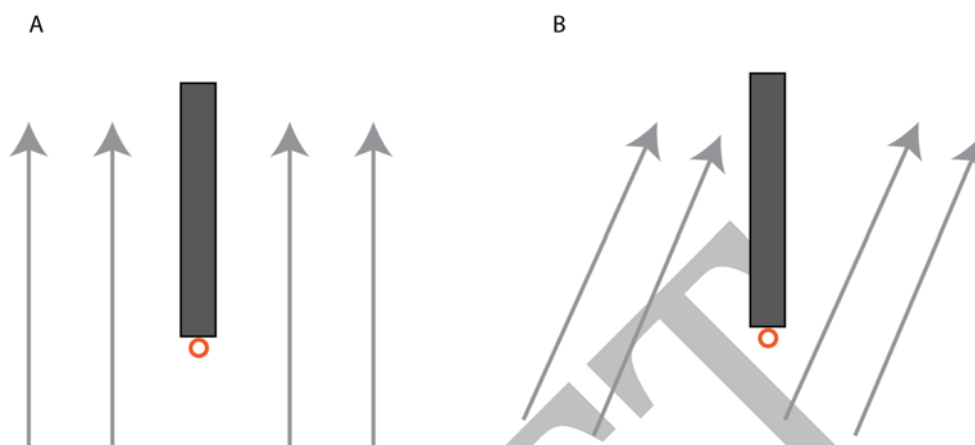


Figure 10: Simplified schematic of air flow changes relative to the LWC-100 sensing element (shown as the orange circle). The LWC is mounted in a rigid position and can-not move relative to the incoming air flow.

920

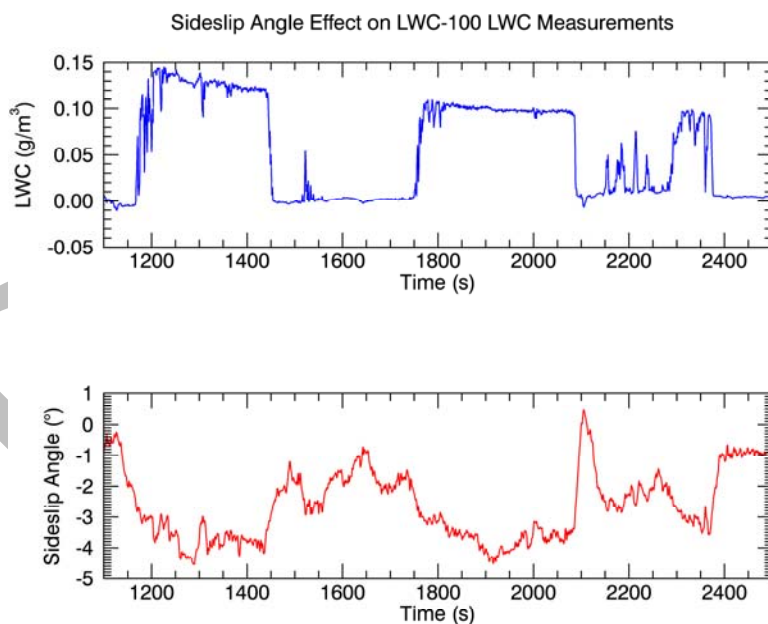
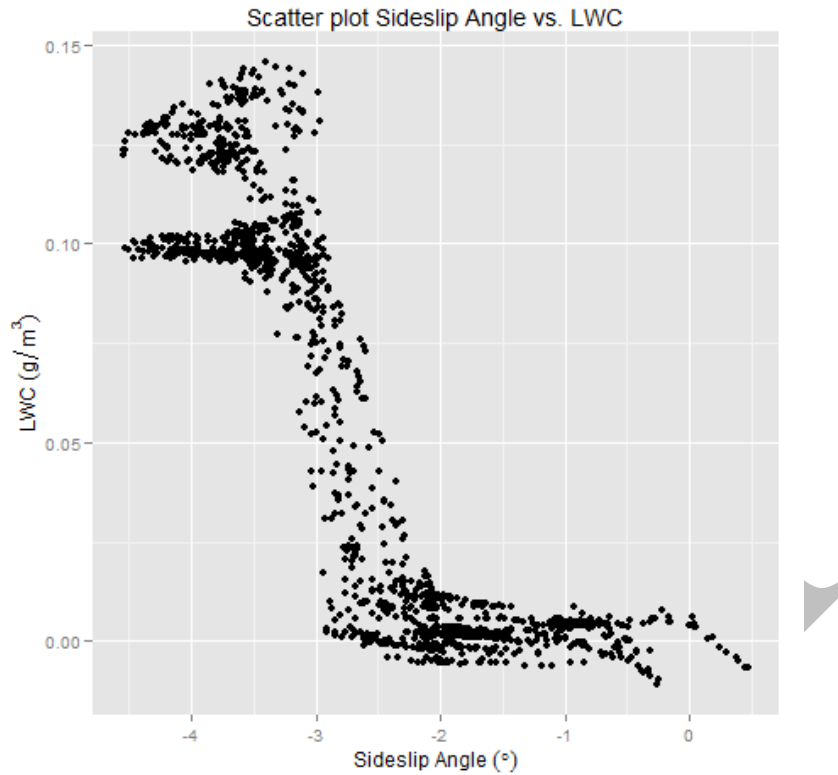


Figure 11: Plot of a segment of the July 9, 2013 calibration flight that occurred mostly outside of cloud. Where the sideslip angle increases negatively there is a noticeable jump in LWC (~ 0.1 to 0.15 g/m^3) measured by the LWC-100.



925 *Figure 12: Scatter plot of the Sideslip Angle vs. LWC for the LWC-100 during the same time period of the same July 9, 2013 flight as in Figure 11 above.*

Calibration of the LWC-100 is accomplished by relating the heat dissipated by the sensor wire in dry air to the analog output voltage. Outside of cloud, the power consumed by the sensor wire is solely due to convective heat loss by air
930 flowing around the sensor wire. This term is then assumed to remain constant for flight legs at a constant altitude and airspeed, even in cloud. The relation in (6) for the Nusselt Number is then used in conjunction with the relation of the power dissipation by the hot-wire (for the wet and dry air terms) given by (4) and the
935 power delivered to the hot-wire given in (7). This relation is then used in a guess-and-check iterative convergence algorithm in MATLAB, developed at the University of Wyoming by Dr. Al Rodi. The algorithm first calculates the baseline temperature

of the sensor wire at a given constant altitude out of cloud then calculates appropriate temperature coefficients that refine the in cloud dry air power term for a given airspeed. However, there is a limitation. In order for the code to provide reasonable temperature coefficients there needs to be a certain amount of data points that are out of cloud, typically on the order of XX% to XX%. For COPE each of the research flights contained enough out of cloud data points in order to obtain a good calibration.

3.1.1.2 THE NEVZOROV LWC/TWC PROBE

The Nevzorov probe provides yet another improvement to the King type hot-wire LWC probe. The Nevzorov Total Water Content (TWC)/Liquid Water Content Probe (LWC) was originally developed in the Cloud Physics Laboratory of the Russian Central Aerological Observatory in the mid-1970s. It is a hot-wire instrument that has two main sensor wires that are held at a constant temperature. The Nevzorov operates on the same principle as the LWC-100 but has the capability to measure both the LWC and the total condensed water, TWC. This makes it particularly useful for measurements in mixed phase clouds, allowing for estimates of the phase discrimination in those clouds. Under ideal conditions, especially that of cirrus and other high ice-content clouds where there is little LWC present, this allows for the calculation of Ice Water Content (IWC) by subtracting the measured LWC from the measured TWC. During COPE, this calculation wouldn't work. In fact,

960 in some cases the values of TWC were lower than the LWC due to the uncertainties
in collection efficiencies of each sensor.

Like the LWC-100 the LWC (and the TWC) is calculable from first principles
from the heat dissipated by the liquid or ice impacting the sensor wires. However,
unlike the LWC-100, the Nevzorov probe also has a reference wire for each sensor
965 type that allows for the direct measurement of the dry air term. As discussed in the
previous section, this value must be calculated for the LWC-100 probe using an
iterative guess-and-check algorithm and requires more out-of-cloud data points
than in cloud.

The basic schematic of the Nevzorov probe is shown in Figure 13. It consists
970 of a movable vane that allows the sensors to pivot parallel to the incoming air flow.
This helps achieve the maximum collection efficiency and it also helps prevent
droplets and ice crystals from impacting the reference sensors providing greater
accuracy of the dry air term in cloud. The vane also typically has a leading edge,
heated wire to prevent icing of the apparatus in super-cooled clouds (Korolev et. al.
975 1997).

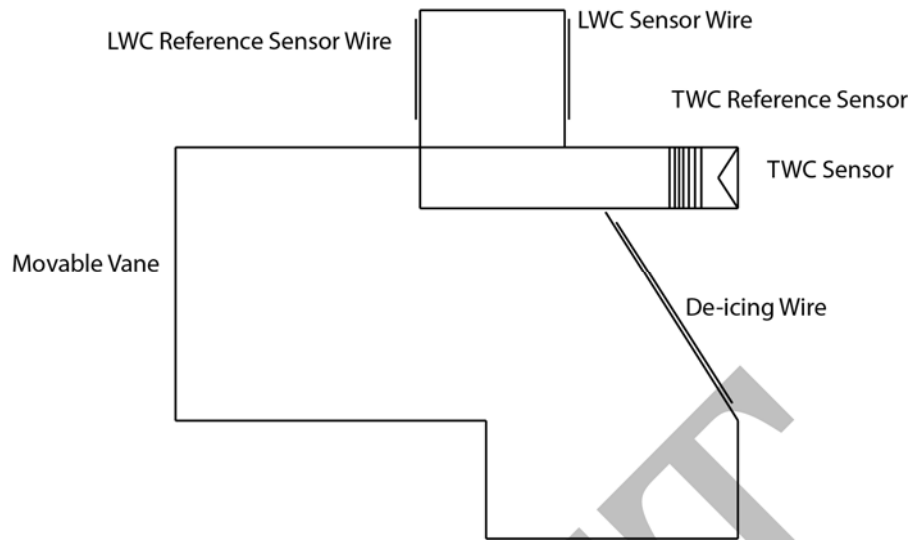


Figure 13: Schematic of the standard design of the Nevzorov LWC/TWC probe.

The Nevzorov probe hot-wire sensor wires are made of single-layer enamel-covered nickel wire wound tightly around a solid copper rod and then cemented to the opposite edges of a flat plastic plate (that is part of the vane assembly). The diameter of the sensor wire and rod assembly is 1.8 mm and the length is 16 mm. The LWC sensor wire operates in a similar manner as the LWC-100. At 90° C the sensor wire resistance ranges between 2.5 and 3.5 Ω (Korolev, et. al., 1997). The LWC sensor wire is also inherently designed such that ice particles will impact, shatter, and split away from the sensor's convex surface, with minimal transfer of heat. Liquid water will form a thin film on the wire and evaporate with a greater heat loss (Korolev, et. al., 1997).

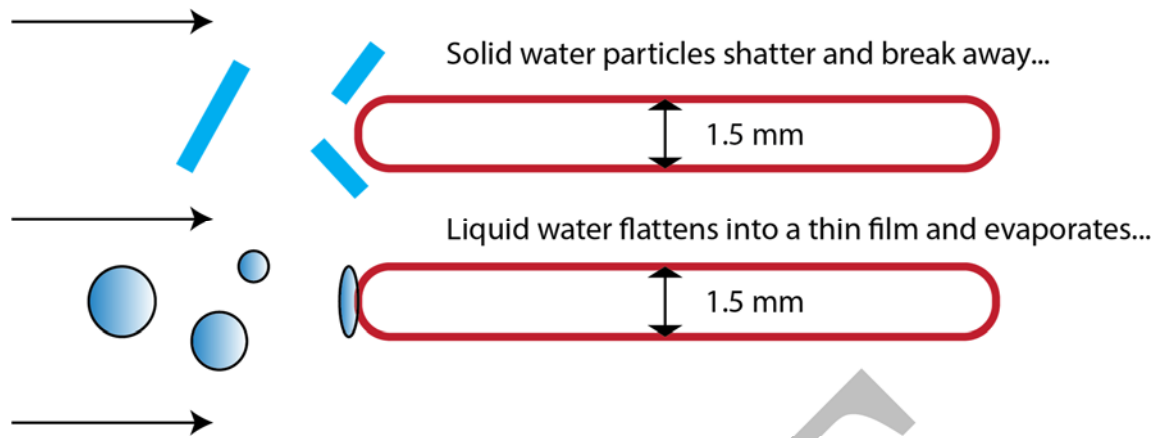


Figure 14: The LWC sensor's phase discrimination capability. The solid ice particles shatter and deflect away from the wire wrapped cylinder's convex surface with minimal heat loss (figure reproduced from Korolev, et. al. 1997).

The LWC sensor wire can capture most moderately sized droplets, however it suffers from the same limitation the LWC-100 where, as larger droplets impinge on the sensor wire, some fraction of the liquid sheds prior to complete evaporation. The collection efficiency of the LWC sensor wire approaches 100% for diameters between $10\ \mu\text{m}$ and $100\ \mu\text{m}$ and then decreases significantly, mostly due to mass shedding during evaporation (Biter et. al., 1987). The Nevzorov probe that was flown on the UWKA for COPE-MED had two LWC sensor wires in order to achieve LWC measurement redundancy. The single reference wire that is standard for the LWC on the Nevzorov probe was used for both these sensor wires.

The TWC sensor is a conical plastic tube collector with the hot-wire coil attached at the end of the cone's apex. The hot-wire coil inside the cone is mounted in a spiral configuration such that the entire surface of the inner cone is a hot-wire sensor. Anywhere a particle impacts on the cone's inner surface it is in contact with a hot-wire sensor. The reference wire for the TWC sensor is attached to a groove on the side of the sensor tube itself. Figure 15 shows a schematic of the TWC sensor

and a depiction of how its design allows for collection of water droplets and its
ability to capture and melt ice crystals in order to determine the TWC.

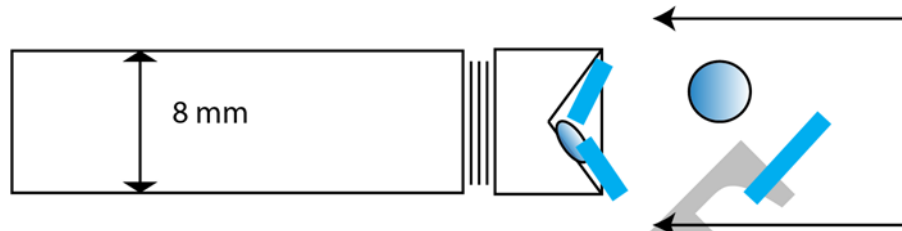


Figure 15: Depiction of how the TWC Probe collects both solid and liquid water particles in order to determine total water content. Liquid water droplets are captured in the cone and form a thin film and evaporate. Solid ice particles shatter and collect in the cone and melt. (Figure reproduced from Korolev, et. al., 1997)

The original design has a cone apex angle of 120° . This configuration, however, was more susceptible to particles being ejected from the cone prior to melting or evaporating. In order to increase the collection efficiency of the Nevzorov probe a design of a “deep cone” with an apex angle 60° was created that allowed for a greater probability of multiple bounces of incoming particles before they are ejected from the cone. This “deep cone” design was flown on the UWKA during COPE-MED. This deeper cone design increases the collection efficiency (Korolev, et. al., 2013).

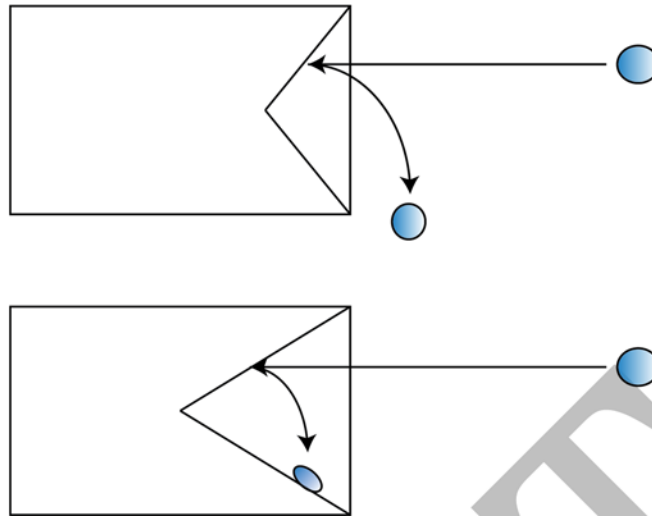


Figure 16: Schematic of the difference between how the shallow cone and deep cone designs of the Nevzorov probe's TWC sensor react to liquid water droplet impacts. The deeper cone design allows for more bounces and a greater probability that the particle will not escape the cone through bounces. (Figure reproduced from Korolev, et. al., 2013).

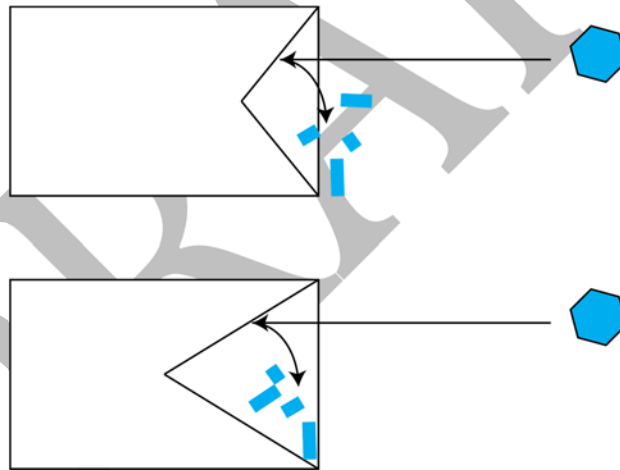


Figure 17: Schematic of how the shallow vs. deep cone designs handle ice shattering & bouncing.

Figure 18 shows the schematic of a typical Nevzorov probe electronic control circuit. This circuit is somewhat more advanced than the LWC-100's. Both the main collector sensor and reference wires form two temperature-dependent legs of a wheatstone bridge circuit with amplifiers. The adjustable resistors R' and R'' in the

figure are mounted on the control box and are used to set the temperature of each
 1040 sensor wire. Laboratory calibrations determine the relationship required between
 R' , R'' and the required temperature (Korolev et. al., 1997).

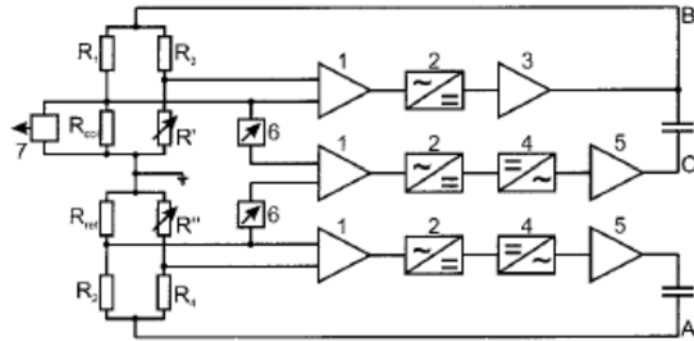


Figure 18: Nevzorov Probe control circuit (adapted from Korolev, et. al., 1997).

The calibration of the Nevzorov LWC and TWC probes requires flying flight
 legs at a constant altitude in order to get a baseline reading for the reference
 sensors and the LWC and TWC sensing wires. These data are then used to determine
 clear air corrections to the sensor wire to match the reference wire. This was done
 1050 for the COPE-MED campaign using 3 flight levels. At each level five, straight and
 level runs were performed for ~1 minute at three different flight speeds. The flight
 levels chosen to calibrate the Nevzorov probe for COPE-MED were 23,000 ft, 13,000
 ft, and 3,000 ft.

Under ideal conditions the LWC probe wire will measure a value of 0 g m^{-3}
 1055 in dry, cloud free air (Korolev, et. al., 1997). However, due to the sensitivity of a hot-
 wire probe to convective heat losses, this value will drift. There are several sources
 of drift. Drift that can occur due to changes in airspeed, external temperature

changes, changes in pressure (altitude), and random fluctuations in clear, non-cloudy air. The random fluctuations of straight and level flight are estimated to be $\pm 0.002 \text{ g m}^{-3}$, which is an order of magnitude less than the King probe. The internal circuitry is designed to compensate for larger random fluctuations and Korolev, et. al. tested the other sources of drift in their 1997 paper. Table 2 quantifies the three major sources of drift. Since each has an order of magnitude of 10^{-3} the error induced from these is considered negligible (Korolev, et. al. 1997).

Table 2: Magnitudes of baseline drift of the LWC in the Nevzorov LWC/TWC probe due to various sources.

Temperature Drift	$\sim 0.5 \times 10^{-3} \frac{\text{g}}{\text{m}^3 \text{ } 10^\circ\text{C}}$
Pressure/Altitude Drift	$\sim 5 \times 10^{-3} \frac{\text{g}}{\text{m}^3 \text{ km}}$
Airspeed Drift	$\sim 3 \times 10^{-3} \frac{\text{g}}{\text{m}^3 \text{ } 10 \text{ m s}^{-1}}$

The Nevzorov LWC sensor coils suffer from the same droplet size limitations as the LWC-100. Lower collection efficiency at smaller sizes and incomplete evaporation and shedding at larger sizes. For the TWC sensor, one needs to consider the Aerodynamic Equivalent Diameter (AED) of irregularly shaped ice particles. The AED is defined as the diameter of a unit density sphere that would have the identical settling velocity as the irregularly shaped particle. All particles with AED smaller than a certain critical size will tend to follow the streamlines. Therefore, there remains an issue where the smaller ice particles, and smaller spherical droplets, will tend to flow around the sensor. To a first approximation

these small crystals should have a collection efficiency similar to those for small water droplets of equivalent mass (Korolev et. al. 1997). Generally for particles 20 μm , or larger, the collection efficiency is found to be greater than 80%. The collection efficiency for small liquid droplets is given by:

$$\epsilon = \frac{d_{\text{eff}}^2}{d_{\text{eff}}^2 + d_0^2} \quad (10)$$

(Nevzorov and Shugaev 1992a) where $d_{\text{eff}} = 3 \frac{\text{LWC}}{\rho_l G}$ (G is the extinction coefficient and ρ_l is the density of liquid water) and $d_0 = 7.5 \mu\text{m}$ for the TWC sensor and $d_0 = 1.7 \mu\text{m}$ for the LWC at nominal aircraft speeds (Korolev, et. al., 1997).

3.1.2 OPTICAL PARTICLE COUNTER PROBES

Optical particle counters (OPCs) are a class of in-situ microphysics probe that infer the size of a particle by measuring the intensity of light scattered by that particle from a monochromatic laser beam. Within certain solid angular limits the response measured by a photo detector is a direct measurement of the particle's size, assuming a mostly spherical particle and a specified dielectric constant. These types of in-situ probes cover a broad range of particle sizes up to several tens of microns. However, the response of these photo detectors to monochromatic light is generally non-monotonic. Thus, identical measured responses can, in some cases, be attributed to multiple sizes of particles. This non-monotonic behavior is due to the

Mie resonances, or bumps, which are dependent on the sizes, shapes, and refractive indices of the incident particles. It can also heavily depend on the optical geometry of the probe itself. The suppression of these resonance effects may be partially accomplished by using a multimode laser.

OPC's are droplet-sizing instruments, not LWC-measuring probes, so rather than measuring LWC directly, LWC is derived by summing over the size bin distributions. Given a binned particle size, n_i , the LWC is derived from the third moment as shown in a variation of equation 2 where N is the total number of instrument channels (or bins):

$$\text{LWC} = \frac{4}{3} \pi \rho_l \sum_{i=1}^N \frac{n_i r_i^3}{V_{\text{sample}}} \quad (11)$$

where V_{sample} is the sample volume, which depends on the geometry of the laser, airspeed, and the sample time.

3.1.2.1 THE FORWARD SCATTERING SPECTROMETER PROBE

The Forward Scattering Spectrometer Probe (FSSP) (Knollenberg, 1976) was originally manufactured by Particle Measuring Systems Inc. out of Boulder, CO and has been one of the most widely used in-situ probes for measuring cloud droplets over the last few decades. The FSSP detects, counts, and sizes single particles, and sizes them, by measuring the intensity of the light scattered by particles passing

through a hybrid HeNe laser beam focused at the center of an inlet tube that faces
 1120 into the oncoming airstream as seen in Figure 19.

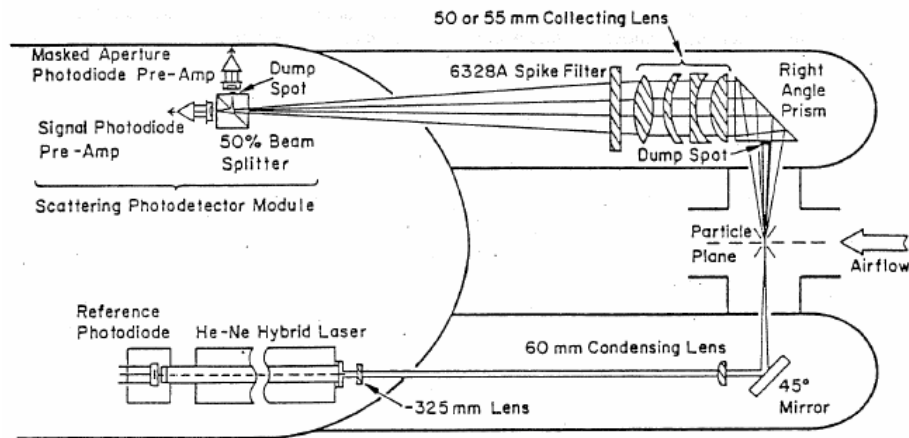


Figure 19: Schematic of the optical configuration of the FSSP single particle scattering probe (figure adapted from <https://www.eol.ucar.edu/instruments/forward-scattering-spectrometer-probe-model-100>).

The FSSP laser has a beam diameter of about 200 μm at its focal point. Laser
 light that is scattered in the forward direction is directed by a right angle prism
 positioned about 38 mm away from the particle plane though a compound
 1130 condensing lens. This lens focuses the beam into a beam splitter onto a pair of
 photo-detectors. The "dump spot," in Figure 19, is a beam block on the opposite side
 of the inlet, which prevents direct light from the laser from entering the collection
 optics and corrupting the scatter signal (Pinnick et al. 1981).

Mie scattering theory, which assumes a plane wave scattering from spherical
 1135 particles, is used to relate the scattering intensity to the particle size. The response
 function is obtained by integration over a scattering angle range of α° to β° :

$$R(x) = \frac{\lambda^2}{2\pi} \int_{\alpha}^{\beta} \left(|S_{\parallel}(\theta, m, x)|^2 + |S_{\perp}(\theta, m, x)|^2 \right) \sin \theta d\theta \quad (12)$$

where λ is the wavelength of the laser, S is the parallel and perpendicular components of the the complex scattering function, m is the complex index of refraction, $x = \frac{\pi D}{\lambda}$ is a dimensionless size parameter for a particle of diameter D , and θ is the scattering angle (Barnard & Harrison, 1988). Liquid particles of refractive index ~ 1.33 are also assumed. Therefore, along with the above and the FSSP's other optical geometric properties, the FSSP has a total collection angle from about $3^\circ - 13^\circ$ (Pinnick, Garvey, & Duncan, 1981). The electronics measure both the height and duration of the pulse created by a particle passing through the beam.

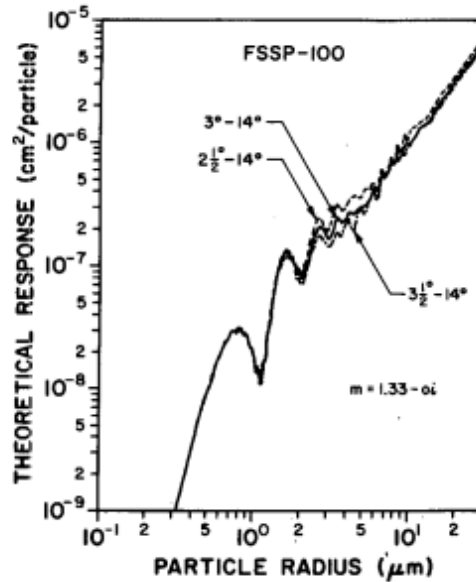


Figure 20: theoretical response of the FSSP for $m = 1.33$ and various angle pairs α and β in (12) (Pinnick, Garvey, & Duncan, 1981).

The probe's optical depth of field (DOF) is used to select droplets crossing the center of the beam, those close to its focal point in the middle of the sampling tube. This is accomplished by optically masking one of the detectors and the use of
1155 real-time electronics. The masked detector only receives scattered light when the particles pass through the laser beam displaced greater than ~ 1.5 mm on either side of the center of beam's focus. When the pulse from that masked detector exceeds that from the unmasked detector the particle is rejected as being outside of the DOF. Among the DOF selected droplets, there is an additional rejection criteria.
1160 Particles are rejected by comparing their electronic pulse duration to the mean pulse duration. The mean pulse duration is a linear running average of the DOF selected pulse duration. If the pulse duration is shorter than the mean, then the particle is rejected. If it is the same or longer, the particle is accepted. This criteria is called the velocity average control (VAC) and allows for rejection of particles that
1165 pass through the beam edge as illustrated in Figure 21.

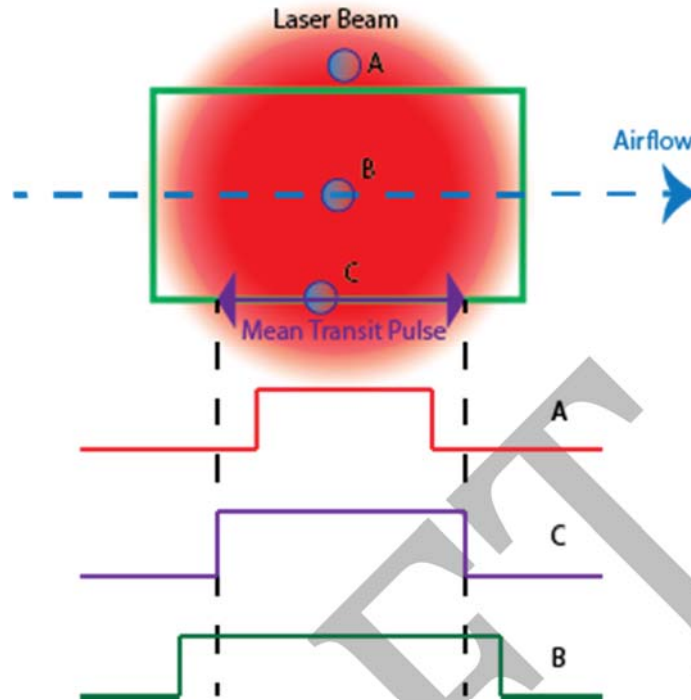


Figure 21: Schematic of the VAC acceptance criteria of the FSSP. The green box, which covers 62% of the beam's diameter, represents the acceptance range. Particle A crosses the beam close to the beam edge and its pulse (red) is shorter than the mean, so it is rejected. Particle B is within the acceptance region and has a pulse longer than the mean (green). Particle C is on the mean pulse region (purple) and is also accepted. (based upon figure 1 in Coelho, et al. 2005)

Both criteria are required due to the fact that the FSSP's multimode laser spot does not have a uniform intensity and particles near the edges may be undersized. However, the VAC assumes the pulse duration only depends on the location of the particle trajectory with respect to the beam and not on the particle size, making the VAC criteria most efficient for monodisperse spectra. Larger droplets in non-monodisperse spectra can produce statistically longer pulses so the FSSP has a delay mode that can reduce the dependence of the pulse duration on the droplet size by measuring the pulse duration at the mid-pulse amplitude (Coelho et al. 2005). Round-off errors on the shorter transit time measurement of droplets

crossing the beam edge also affect the VAC selection criteria since it is generally limited to 10 Hz (Dye and Baumgardner 1984).

1185 Due to the geometry of the probe and associated optics – roughly 80% of the
particles are rejected as being outside of the DOF. Of the remaining 20% of accepted
particles roughly half of those are rejected due to the VAC criteria. The remaining
10% of the particles are then sized by the electronics. After sizing, the particles are
1190 range 2 μm to 47 μm . The size of the particle is determined from the pulse height by
comparing it to a predetermined set of pulse heights forming the upper limits of the
15 size channels and registering a count into the appropriate channel. Counts taken
over a period of time are aggregated to generate a drop size distribution. However,
since the laser beam intensity is not uniform the intensity of scattered light by
1195 particles passing through the beam is highly dependent on the path they take
through the beam. This beam inhomogeneity tends to produce broadening of the
measured droplet spectrum (Baumgardner and Spowart 1990). The accuracy of the
particle by particle diameter measurements of the FSSP is on the order of $\pm 20\%$,
due mostly to particle positioning within the beam.

1200 The overall accuracy of the derived concentration by the FSSP is on the order of
 $\pm 16\%$ (Baumgardner, 1996).

 Since the liquid water content is not a measured quantity by the FSSP, but
rather a derived quantity obtained by integrating the size distribution measured by
the FSSP, uncertainties in the size measurements can lead to root sum squared
1205 errors in the liquid water content of up to a factor of three higher. There are two

fundamental measurement uncertainties that impact the FSSP measurements. The first is shattering of liquid and ice particles impacting the shroud that can lead to miscounts. This is especially the case when precipitation sized ice particles are present (Korolev et al. 2011, 2013). The second is optical and electronic coincidence errors. Optical coincidence results from multiple particles spaced close together such that they enter the laser beam and scatter as if they were a single, irregularly shaped particle. Electronic coincidence (or dead time) is defined as particles entering the laser during electronic reset time and thus not being detected properly. The probability of optical and electronic coincidence error increases with concentration. The probability is $\sim 5\%$ losses at 300 cm^{-3} to greater than 30% at 1000 cm^{-3} . Generally, algorithmic corrections are applied to account for these losses (Baumgardner et al. 1985; Brenguier et al. 1989; Brenguier et al. 1994).

FSSPs are typically calibrated by the use of monodispersed glass beads. More recently FSSPs have been calibrated, with larger success, by using a stream of monodisperse water droplets (Korolev 1985). Figure 22 shows the different Mie (theoretical response) curves for the glass beads vs. liquid drops. Figure 22 shows the differences in the Mie curves for crown glass beads and liquid water drops. Calibrations require adjusting instrument thresholds in the probe electronics based on beads or drop sizes.

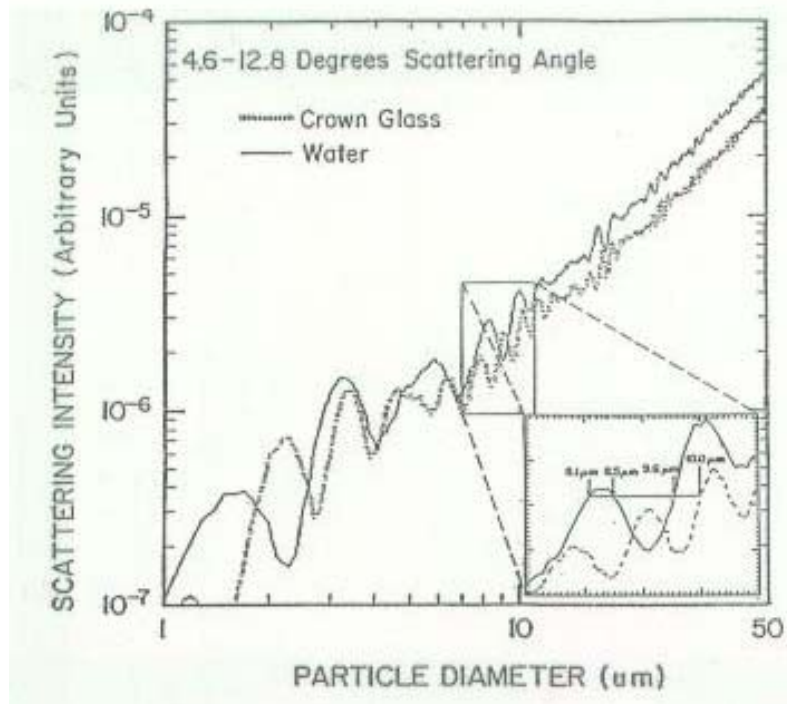


Figure 22: Differences in the Mie curves for crown glass beads (used in the FSSP calibration procedure) and liquid water for the manufacturer's specified scattering angle range (<https://www.eol.ucar.edu>).

1230 In COPE the FSSP was not calibrated prior to deployment. The UWKA
research team rather conducted a check on particle sizing using glass beads. Two
sizes of glass beads $\sim 10 \mu\text{m}$ and $\sim 20 \mu\text{m}$ were used to test the sizing of the FSSP.
These sizes corresponds to $8.9 \mu\text{m}$ and $17.3 \mu\text{m}$ water-equivalent diameter, taking
into account difference between index of refraction between crown glass and water.
1235 Results of these tests suggest the FSSP was oversizing from between $3 \mu\text{m}$ to $5 \mu\text{m}$
(Figure XX).

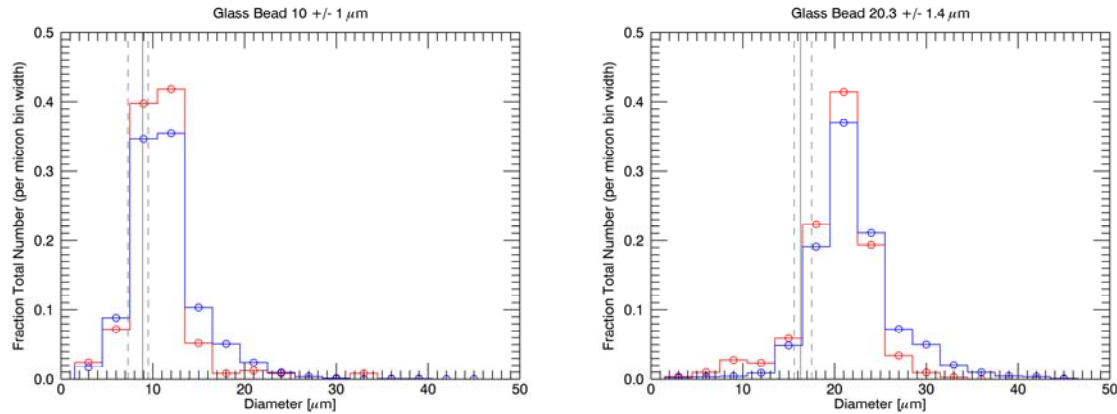


Figure 23: Histograms from the May 08, 2013 glass bead sizing test of the FSSP. The FSSP looks large for the 2 bead tests. The solid grey line represents the expected size reported by the FSSP. The histograms show that the mean value of the bead tests are both larger.

3.1.2.2 CLOUD DROPLET PROBE

The cloud droplet probe (CDP) is also a single particle, forward-scattering optical spectrometer manufactured by Droplet Measurement Technologies. It was developed, in part to improve upon the mechanical design of the FSSP and more importantly to address inherent design issues such as particle shattering. It was also developed to improve upon the other optical and electronic issues that impact the FSSP. Lance, et. al. (2010) made some design and calibration improvements that also serve to improve the results of measurements by the CDP.

The CDP is able to measure size distributions of cloud liquid water droplets in a similar manner to the FSSP. One marked difference is that the CDP uses a 658 nm, single spatial and longitudinal mode, diode laser. The advantage of using a single mode laser is that it is more spatially coherent and avoids the larger intensity, inherent phase inhomogeneities that are found in a multimode laser (Siegman

1996). Figure 24 illustrates an ideal Gaussian beam profile, the CDP's beam profile will be close to the idealization but not as symmetric. The CDP's beam is an elliptical Gaussian beam, anamorphic because the beam diverges in the two perpendicular directions, roughly $2\text{ mm} \times 0.2\text{ mm}$ (Lance, et. al. 2010). The single-mode laser also avoids the inability of a multimode laser to be focused to a diffraction-limited spot (Siegman, 1986). The disadvantage of the single-mode laser is that the Mie resonances are generally more pronounced, whereas in a multi-mode laser the Mie bumps are typically damped (Knollenberg et al. 1976).

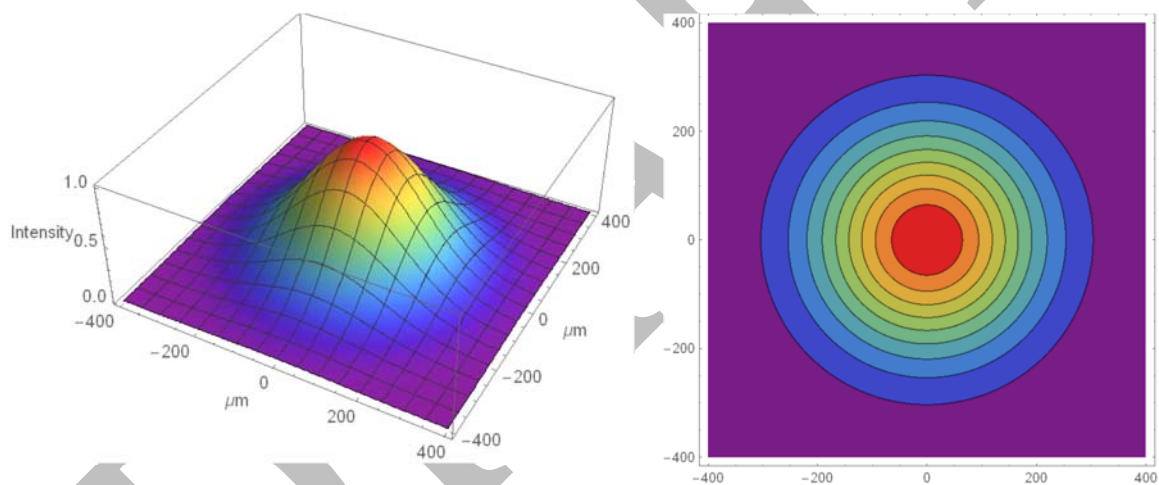


Figure 24: Representation of the CDP's single-mode laser intensity profile. The beam is an elliptical Gaussian, which will have a profile similar to the plot shown. However, this plot is an idealization and the real beam profile isn't as symmetric as shown here because the beam diverges in the two perpendicular directions.

The optical set up of the CDP consists of optics and detectors that are separated into a “qualifier” component and a “sizer” component. A mask with a rectangular slit configuration that allows single slit diffraction patterns to be detected in such a way that the detector can determine if the particle is out of focus or in focus, is used as a mask in the qualifying optics. If the particle is in focus – and

within the depth of field – then it is qualified as being in the sample area. If it is out
of focus it is qualified as being out of the sample area. The sample area of the CDP is
heavily dependent on the optical configuration of the device (Lance, et. al. 2010).
Figure 25 shows the mechanical and optical configuration of the CDP to scale. Figure
26 shows the difference in the signals the qualifier receives when the particle is
within and outside the depth of field.

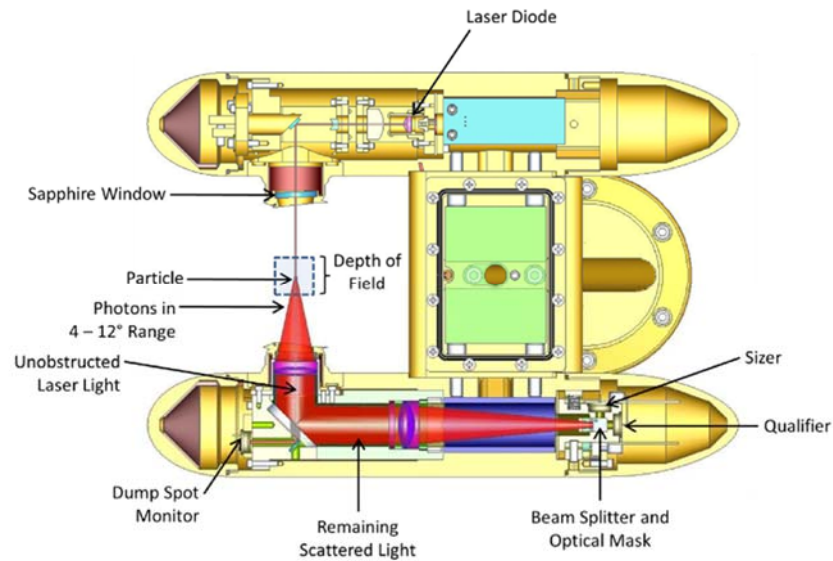


Figure 25: Scale representation of the mechanical and optical set-up within the housing of the CDP (DMT CDP User's manual).

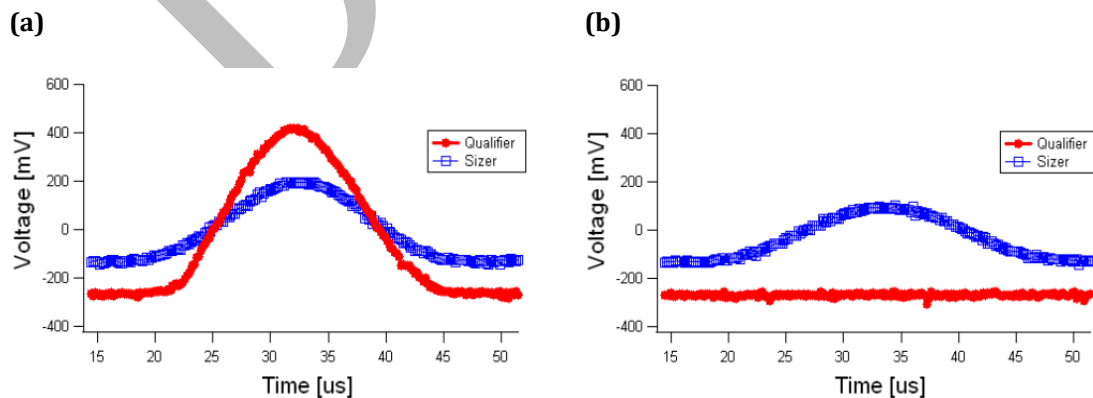


Figure 26: (a) Signals when the drop is in the sample area. (b) Signals when the drop is outside the sample area. (Lance, et. al., 2010)

An un-masked photo detector and a comparator circuit are used for particle sizing (Lance et. al. 2010). The sample area lies within the Rayleigh range of the elliptical Gaussian beam, therefore the beam very closely approximates a plane wave. The light scattered by a droplet within that sample area closely follows Mie scattering theory (Bohren and Huffman, 1983). The digital signal obtained by the sizing optics is related to the particle size. The CDP can measure droplet sizes in the range from 2 – 50 μ m (Lance, et. al. 2010).

Droplet sizes are binned according to size ranges in 30 data bins. The default configuration is for the first bins for sizes between 3 – 14 μ m are 1 μ m wide and the bins from 15 μ m – 50 μ m are 2 μ m wide. There is a non-monotonic relationship between the forward scattered light signal and droplet size, so that the sizing resolution of the CDP is rather limited in its ability to get the fundamental sizing accurate (Lance et. al. 2010). In order to account for the Mie ambiguities seen in OPCs, the UWKA research group combines bins where there are known Mie resonances that lead to such ambiguities. Figure 27 illustrates a schematic of the CDP's data bins and which bins are combined by the UWKA group.

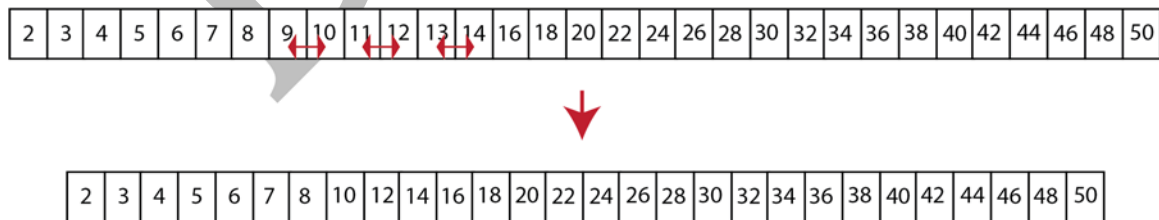


Figure 27: Schematic of the CDP bins. In order to account for the Mie ambiguities the UWKA research group combines certain bins, namely the 9 and 10, 11 and 12, and 13 and 14 size bins. The bin sizes shown here are bin edges and in μ m.

The sample area of the CDP varies with airspeed. The CDP operates most
1310 efficiently in the airspeed ranges of 10 – 200 m/s (Lance, et. al. 2010). The UWKA
typically flies at an average airspeed of 100 m/s, well within this effective range.

The sources of uncertainty in the CDP result from of both optical and
electronic considerations, and though a marked improvement over the FSSP, it still
suffers from some of the same fundamental sources of error as the FSSP. Although
1315 the CDP's single-mode laser avoids the greater spatial intensity and phase
inhomogeneity, the CDP still experiences some broadening of the droplet spectrum
from those effects. Optical coincidence can still cause undercounts or oversizing
errors in the CDP. However, the probability of these types of coincidence errors is
much lower than the FSSP, on the order of less than 5% for concentrations greater
1320 than 500 cm^{-3} , due to the much smaller volume of the CDP laser beam
($\sim 0.06\text{ mm}^3$) compared to the FSSP (Lance et. al. 2010). The CDP used during COPE
had the pin-hole qualifier mask installed, which also significantly reduced
coincidence errors.

Particle shattering is minimized as part of the CDP's inherent design. The
1325 aerodynamic arms upstream of the beam location and its open path help resolve
this. Khanal et al. (2015) show that in ice-only clouds, the effect of ice shattering is
at the CDP particle detection limit. Finally, random statistical uncertainties in
counts, due to the inability to resolve spatial variability in cloud scales smaller than
100 m, will add to the overall uncertainty of the CDP. However, this uncertainty is
1330 less than 5% for concentrations greater than 13 cm^{-3} when given a 1Hz sampling

rate and an airspeed of $\sim 100 \text{ m s}^{-1}$ (Lance, et. al. 2010). During COPE the CDP sampled at both 1 Hz and 10 Hz.

The CDP is calibrated in a similar manner as the FSSP. Prior to COPE, the CDP was calibrated by the manufacturer using the glass bead method and checked in the field periodically in order to ensure proper sizing.. Figure 28 shows the histograms from one of these sizing checks using 10 bead sizes ranging from $2 \mu\text{m}$ to $60 \mu\text{m}$. On average, the CDP sized correctly for the calibrated size range.

1340

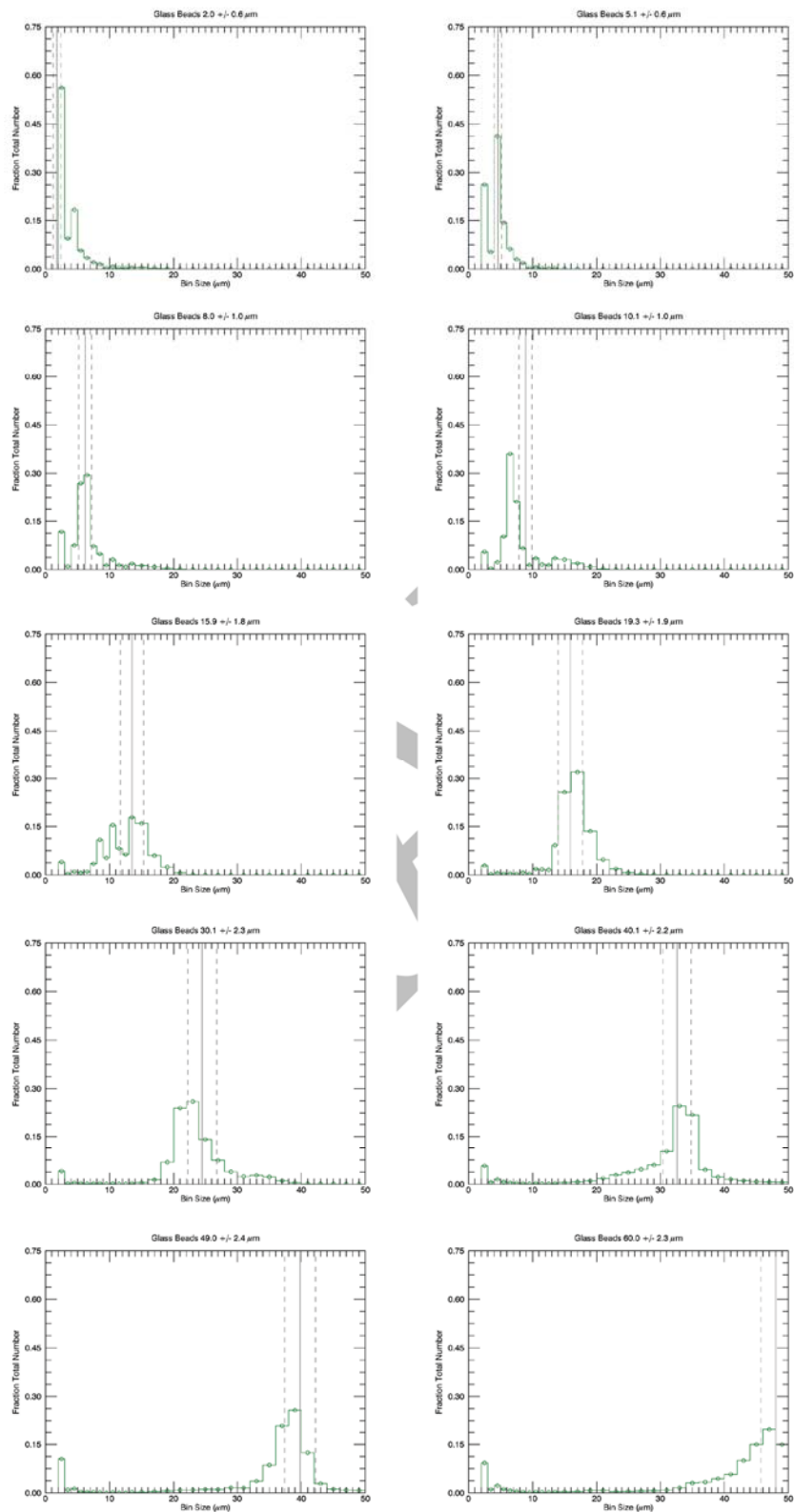


Figure 28: These glass bead sizing tests of the CDP, for 10 different sizes of glass beads show that, on average, the CDP is sizing correctly. As before, the solid grey lines indicate the expected value for that size of glass bead.

1345 3.1.3 LASER DIFFRACTION PARTICLE SIZING PROBES

The laser-diffraction particle-sizing class of optical probes measure laser light scattered by an ensemble of droplets passing through the sample volume of the probe. They are based on a technique originally described by Wertheimer and
1350 Wilcock (1976) where the diffracted light flux collected is proportional to the third power of a spherical particle's diameter. Thus, these types of optical probes can measure LWC directly by effectively using real time "integration" of a volume of particles as they pass through the qualified sample area of the probe.

These probes have the unique capability of making LWC measurements at a
1355 rate that is several orders of magnitude faster than other methods because they can utilize a significantly larger sample volume while measuring an ensemble of droplets (Gerber et. al. 1984). This fast response time allows for investigations of fine-scale behavior of clouds such as in cumulus entrainment (Gerber et. al. 2008).

1360 3.1.3.1 THE GERBER PVM-100A

The Particle Volume Monitor (PVM), model PVM-100A, also colloquially called the Gerber Probe after its primary inventor, is an aircraft mounted version of the original ground-based PVM-100 manufactured by Gerber Scientific, Inc., Reston,
1365 Virginia. The PVM is designed to measure an ensemble of small droplets within an effective volume of about 3 cm^3 by laser diffraction. In this manner, it can directly obtain the liquid water content (LWC) and droplet surface area (PSA) of an

ensemble of cloud droplets. The PVM is also able to derive the droplet effective radius (R_e) via:

1370

$$R_e \propto \text{LWC/PSA} \quad (13)$$

One of the greatest difference in the PVM measurements, from other optical probes, are that its measurements are independent of the airspeed of the aircraft on which the probe is mounted.

1375

The PVM emits a collimated laser beam of 780 nm wavelength directed across a 11.4 cm diameter sample tube that illuminates an effective sample volume of 1.25 cm^3 and scatters in the near forward direction over a half-angle range between $\sim 0.2^\circ$ and 6° . The laser is housed in the larger support cylinder that is mounted on the aircraft fuselage. The angular intensity distribution of the near-forward scatter is then directed into a lens that focuses it onto a cubic beam splitter, splitting the light into two equal beams. The two scatter beams are then each directed into spatially filtered, segmented, multi-element sensors (Gerber, et. al. 1994).

1380

The interference filters on each sensor weight the scattered light in such a way that they are essentially a physical method of mathematically inverting the integral of the incident radiation flux distribution of the forward scatter. The scattered fluxes are directly proportional to the second and third power of the particle size. Therefore, the light that is measured by the sensors can be directly related to the LWC and PSA. In order to obtain the LWC, the varying radial

1385

transmission filters invert the scattered flux into that channel in order to give the integrated particle volume concentration, N_v :

$$N_v \propto \int n(D) D^3 dD \quad (14)$$

The particle volume concentration is then converted into LWC by the simple relationship:

$$LWC = N_v \rho_l \quad (15)$$

The optics are designed to compensate for any vignette effects. The sensors also have a beam block such that the sensor only detects the light scattered in the near-forward direction by the droplets entering into the beam due to the fact that the beam is much narrower than the sensors (Gerber, et. al. 1994). Figure 29 shows a schematic of the optical set-up of the probe.

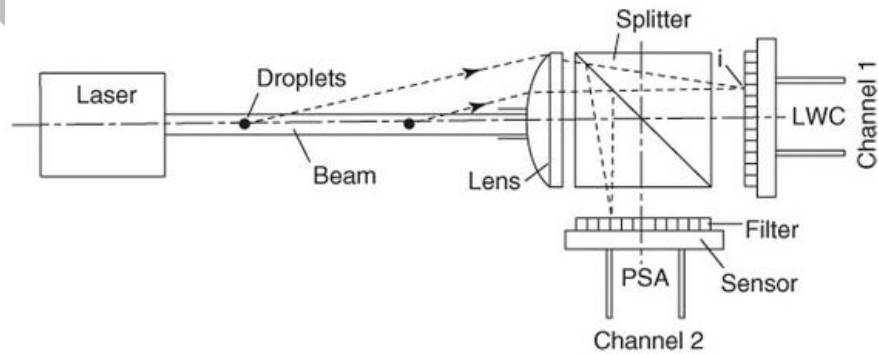


Figure 29: Schematic of the optical set-up of the Gerber probe. Droplets enter the field of the laser beam and scatter the light in a near-forward direction. The light is focused into a beam splitter by the lens and is passed through transmission filters in order to determine LWC and PSA (figure adapted from Gerber, et. al. 1994).

The total flux scattered by the droplets crossing the beam into the photodiodes is given by diffraction theory:

1410

$$F(D) = \sum_{i=1}^N f_i(D) T_i \propto D^3 \quad (16)$$

where T_i is the fraction of transmitted light and $f_i(D)$ is flux of light falling upon an adjacent annular segment of spatial filter. N is the number of adjacent annular sections of the spatial filters. The flux on each annular component of the filter is given by:

1415

$$f_i(D) \propto l_i D^2 [(J_0^2 + J_1^2)_{i1} + (J_0^2 + J_1^2)_{i2}] \quad (17)$$

where the J_n are the Bessel functions of the first kind of n^{th} order and the factor l_i , the fraction of the length of the laser beam that contributes light diffracted by the particles into an annular segment, which compensates for vignetting effects. A filter of this kind gives a theoretical band-pass of droplet sizes between $4 \mu m$ to $45 \mu m$, where the response of the PVM is approximately linear with LWC. This response is close to that of the FSSP. Outside of that range, the PVM's response will gradually roll off with up to a 50% underestimate of LWC at the droplet size extremes of $2 \mu m$ and $70 \mu m$ respectively (Gerber, et. al., 1994). The response of the PVM compared to Mie theory is illustrated in Figure 30.

1420

1425

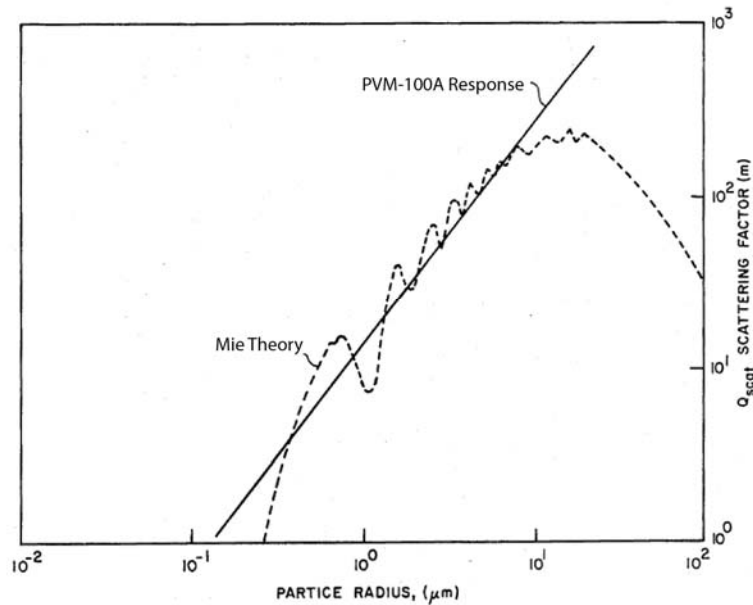


Figure 30: PVM-100A response vs. Mie theory. (Figure adapted from U.S. Patent #4597666).

1430

The accuracy of the PVM is estimated to be better than 10% for droplet spectra with a volume median diameter (VMD) smaller than $30 \mu\text{m}$. For droplets with sizes up to $\sim 60 \mu\text{m}$, the PVM measures LWC in the range $0.02\text{--}10 \text{ g/m}^3$ with an accuracy of $\sim 5\%$. The PVM's overall precision is estimated to be on the order of

1435 0.002 g/m^3 . The PVM is designed to operate in an environmental temperature range of -70°C to 40°C and a humidity range of 0% to 100% (Gerber, et. al. 1994).

The disadvantage of the PVM is that it can be prone to fogging of the optics and that the sensitivity actually begins to drop off at droplets larger than $30 \mu\text{m}$ (Gerber et. al. 1994; Wendish et. al. 2002). Although the PVM has heated optics

1440 designed to prevent fogging it can still experience fogging when the aircraft descends rapidly from very cold temperatures to much warmer, humid air. During COPE, this behavior of the PVM is observed and described in greater detail in

Chapter 4. The loss of sensitivity to droplets larger than $30\ \mu\text{m}$ is a result of convergence of the laser beam. Use of a collimated laser could improve the size sensitivity, but at the cost of the sample volume being reduced and statistical sampling error increasing (Wendish & Brenguier 2013).

The PVM-100A cannot effectively distinguish between ice and liquid particles. The weighting function used for determining LWC is based upon the density of liquid water, so caution should be taken in analysis of data from mixed-phase clouds where the possibility of ice crystals being closer to spherical is higher (Wendish & Brenguier 2013). However, most small ice crystals tend to not be spherical and their exact habit depends heavily on their initiation temperature (Pauppenger and Klett 1997). Therefore, the inability of the PVM-100A to distinguish ice from water should not adversely affect the LWC measured by the PVM appreciably, since the phase function of non-spherical ice crystals is much different than that of spherical liquid water.

Calibration of the PVM-100A consists of adjustment of the baseline of the laser signal using a light diffusing disk and adjusting the PVM's gain to choose a reference voltage for each channel. The condition of the optics can and will adversely affect the baseline signal – e.g. scattering by particulates stuck on the optics – and are typically accounted for during the calibration process.

1465 3.2 SUMMARY

Table 3 below summarizes the probes described in Section 3.1 and provides a brief description of the methodology, the range of LWCs measured, and known
 1470 limitations for each. Figure 31 shows histograms of the measured LWC above a threshold value of 0.02 g m^{-3} for each of the in-situ probes described in Section 3.1. The LWC ranges are noted as being from the manufacturer specification, from the actual COPE data, and/or what the realistic average range for all of the COPE research flights is when taking into consideration corrections or neglecting unrealistic outliers.

1475

Table 3: List of in-situ cloud physics instrumentation installed on the UWKA during COPE.

Instrument	Methodology	COPE LWC Range	Limitations
LWC-100;	Hot-wire method. Calculable from first principles (King, et. al. 1978).	Manufacturer: $0 - 3 \text{ g m}^{-3}$ Data: $0.02 - 2.6 \text{ g m}^{-3}$	Dry air term must be calculated. Flow angle changes not adjusted for in LWC measurements. Only accurate for droplets up to $\sim 50 \text{ }\mu\text{m}$. Collection efficiency issues on small droplet end and shedding and incomplete evaporation on the large droplet end.
Nevzorov LWC/TWC;‡	Hot-wire method. Calculable from first principles & dry air term is directly measured (Korolev et. al., 1997). Deep cone TWC sensor used for COPE (Korolev, 2010).	Manufacturer: $0 - 3 \text{ g m}^{-3}$ Data: $0.02 - 2.3 \text{ g m}^{-3}$	Collection efficiency issues on small droplet end and shedding and incomplete evaporation on the large droplet end.

‡ The Nevzorov LWC/TWC probe was provided by Alexi Korolev for COPE and is not part of the standard suite of in-situ instrumentation installed aboard the UWKA.

FSSP-100;	Single particle forward optical scattering spectrometer. Measures cloud droplet size spectra in 15 channels with lower and upper limits typically set at 1.5 and 47.5 μm . CLWC directly derivable from spectra (Vali et al., 1998; Brenguier et al., 1998).	Data: $0.02 - 7.8 \text{ g m}^{-3}$. Realistic average for all RFs: $0.02 - 3.7 \text{ g m}^{-3}$.	Particle shattering on the inlet shroud. Uncertainties due to coincidence and dead-time errors must be adjusted for by post-processing algorithms. Mie ambiguities lead to multiple sizes for a given response pulse.
CDP; [§]	Single particle forward optical scattering spectrometer. Measures cloud droplet size spectra within 2–50 μm (30 channels) CLWC directly derivable from spectra (Lance et. al., 2010).	Data: $0.02 - 3.5 \text{ g m}^{-3}$.	Uncertainties due to coincidence and dead-time errors must be adjusted for by post-processing algorithms. Mie ambiguities lead to multiple sizes for a given response pulse which are corrected for by bin combination.
PVM-100A;	Measures the optical response of 780 nm diode laser to a volume of droplets with sizes up to ~60 μm . Has an effective sample volume of 1.25 cm^3 (Gerber, et. al., 1993).	Manufacturer: $0.002 - 10 \text{ g m}^{-3}$ Data: $0.02 - \sim 9 \text{ g m}^{-3}$. Realistic average for all RFs: $0.02 - 3.6 \text{ g m}^{-3}$.	Requires careful calibration. Prone to optical fogging under certain extreme changes of environmental conditions. Sensitivity decreases for particles larger than 30 μm . Inability to distinguish ice from liquid water in certain, rare instances.

[§] All improvements, except the water droplet calibration procedure, mentioned in Lance et. al. (2010) were implemented on the CDP installed on the UWKA during COPE.